Geomechanics for Energy and the Environment 38 (2024) 100562

Contents lists available at ScienceDirect

Geomechanics for Energy and the Environment

journal homepage: www.elsevier.com/locate/gete

A preliminary investigation on the mechanical behaviour of a stiff Italian clay in the context of hydrogen storage

Andrea Ciancimino [a,*,1], Renato Maria Cosentini [a,2], Sebastiano Foti [a,3], Alessandro Messori [b,4], Hidayat Ullah [a,5], Giorgio Volonté [b,6], Guido Musso [a,7]

[a] Politecnico di Torino, Turin, Italy
[b] Eni SpA, Milan, Italy

ARTICLE INFO

Editors-in-Chief: Professor Lyesse Laloui and Professor Tomasz Hueckel

Keywords:
Underground hydrogen storage
Depleted reservoirs
Cyclic triaxial tests
Strain rate
Stiff structured clay
Wave measurements
Fatigue loading

ABSTRACT

The large-scale use of renewable energy sources is closely linked to the ability to store excess energy generated during periods of overproduction for use when demand is at a peak. Storing green energy is therefore a key component in the move towards a carbon-neutral economy. Underground hydrogen storage in depleted oil and gas reservoirs may provide an efficient long-term solution. Cyclic injection and production of hydrogen alter the chemo-hydro-mechanical conditions of the reservoir and caprocks, and possible geomechanical consequences of such alterations must be preliminarily assessed for safe storage operations. This study aims at exploring the possible effects of cyclic mechanical loads, such as those that might be induced by hydrogen storage and production, on the mechanical behaviour of a clayey caprock. A series of triaxial tests, both monotonic and cyclic, were carried out on undisturbed samples of a stiff Italian clay cored from a caprock formation overlying a hydrocarbon reservoir. The results show that the material response is characterized by the distinctive stress-strain behaviour of stiff clays, with a rather high fragility, which was found to be highly dependent on the loading strain rate. During laboratory experiments conducted at frequencies larger than in situ ones, cyclic loading under stress control causes a gradual degradation of the material structure leading to the formation of a clear shear band followed by a reduction in shear strength. Eventually, failure occurs as the peak shear strength approaches the applied load. The progressive destructuration also implies a reduction in P- and S-wave propagation velocities and a significant change in the signal shape, which is therefore a promising parameter for monitoring the material degradation process.

1. Introduction

The development of renewable energy technologies is increasing in response to the growing global demand for clean and sustainable energy. However, the inherently intermittent nature of green energy poses a significant challenge to its effective use and inevitably limits its application as a primary source of power supply[1] (see also Fig. 1a). The balancing of supply and demand cycles over seasonal and annual timescales is therefore essential for the large-scale integration of renewable energy sources.[2]

Hydrogen has emerged as a promising solution for efficient energy storage, offering high energy density, versatility and compatibility with various conversion technologies.[4,5] Surplus renewable energy can be converted to "green" hydrogen by electrolysis with no direct carbon emissions, making it a clean and sustainable option for energy storage.[6-8] Alternatively, "blue" hydrogen can be produced by steam

* Corresponding author.
E-mail address: andrea.ciancimino@polito.it (A. Ciancimino).
[1] 0000-0001-8955-4605
[2] 0000-0002-7080-2186
[3] 0000-0003-4505-5091
[4] 0000-0001-5213-3962
[5] 0009-0009-0377-8604
[6] 0000-0002-6942-7198
[7] 0000-0003-3151-4058

https://doi.org/10.1016/j.gete.2024.100562
Received 21 September 2023; Received in revised form 1 March 2024; Accepted 29 April 2024
Available online 4 May 2024

methane reforming which results in carbon dioxide (CO_2) production, requiring additional carbon capture and storge programs.[9,10] While blue hydrogen production is more carbon intensive than green hydrogen, the use of carbon capture techniques allows a significant reduction in net emissions. Hydrogen (blue and green) used as an energy carrier will be a key component in the transition to a carbon-neutral economy.[11-13]

Hydrogen has a high calorific value per unit mass (i.e., about 33.3 kWh/kg). However, its particularly low density poses significant challenges for its efficient storage. For example, under typical reservoir subsurface conditions (i.e. 200 bar and T < 150 °C), hydrogen has a volumetric calorific value of approximately 530 kWh/m^3, about five times less than natural gas.[14] Therefore, surface hydrogen storage is limited to small-scale applications. Underground gas storage facilities are instead more suitable for balancing the large energy fluctuations associated with the seasonality of renewable energy sources.[15,16] In fact, the density of hydrogen, which is 0.084 kg/m^3 at surface conditions, increases with increasing pressure to about 10 kg/m^3 at 200 bar.[3] Nevertheless, large amounts of storage are required to compensate for the intermittent nature of renewables. For example, Stone et al. [17] report a hydrogen storage requirement of approximately 1930 million m^3 for the UK alone, calculated on a seasonal basis and equated on an energy basis.

Among the different types of underground gas storage, salt caverns represent a viable option in the medium term due to their high production rates.[18] However, their use is limited by the existence of suitable geological formations of appropriate size. Depleted oil and gas reservoirs and saline aquifers have emerged as flexible and effective solutions for hydrogen storage due to their large storage capacities and worldwide availability.[3] The process involves a porous formation, which acts as a natural reservoir, and a low-permeable caprock formation, which prevents gas from migrating, along with the lateral trapping structure. During periods of overproduction, hydrogen is injected into the porous formation, displacing the field fluids. These typically consist of brine or residual hydrocarbons in saline aquifers and depleted reservoirs, respectively. To maintain the desired pressure and ensure effective production rates when energy demand peaks, a volume of gas, usually referred to as cushion gas, is intentionally left in the reservoir. The remaining hydrocarbon itself can form such a cushion gas in depleted fields. The proven ability to prevent gas migration over long periods of time is an additional benefit of using exhausted reservoirs.[19] In this sense, the geological formations that constitute the caprock and the reservoir have already been extensively investigated due to the previous hydrocarbon production operations. Some of the infrastructure implemented to carry out the operational phases of the reservoir can also be partially reused, including the injection and production wells, the surface facilities, and the pipeline network. The reuse of depleted hydrocarbon fields can therefore represent a cost-effective efficient solution for underground hydrogen storage.

However, some specific potential issues have to be prevented and monitored while storing gas in depleted reservoirs (e.g., [20]). For one,

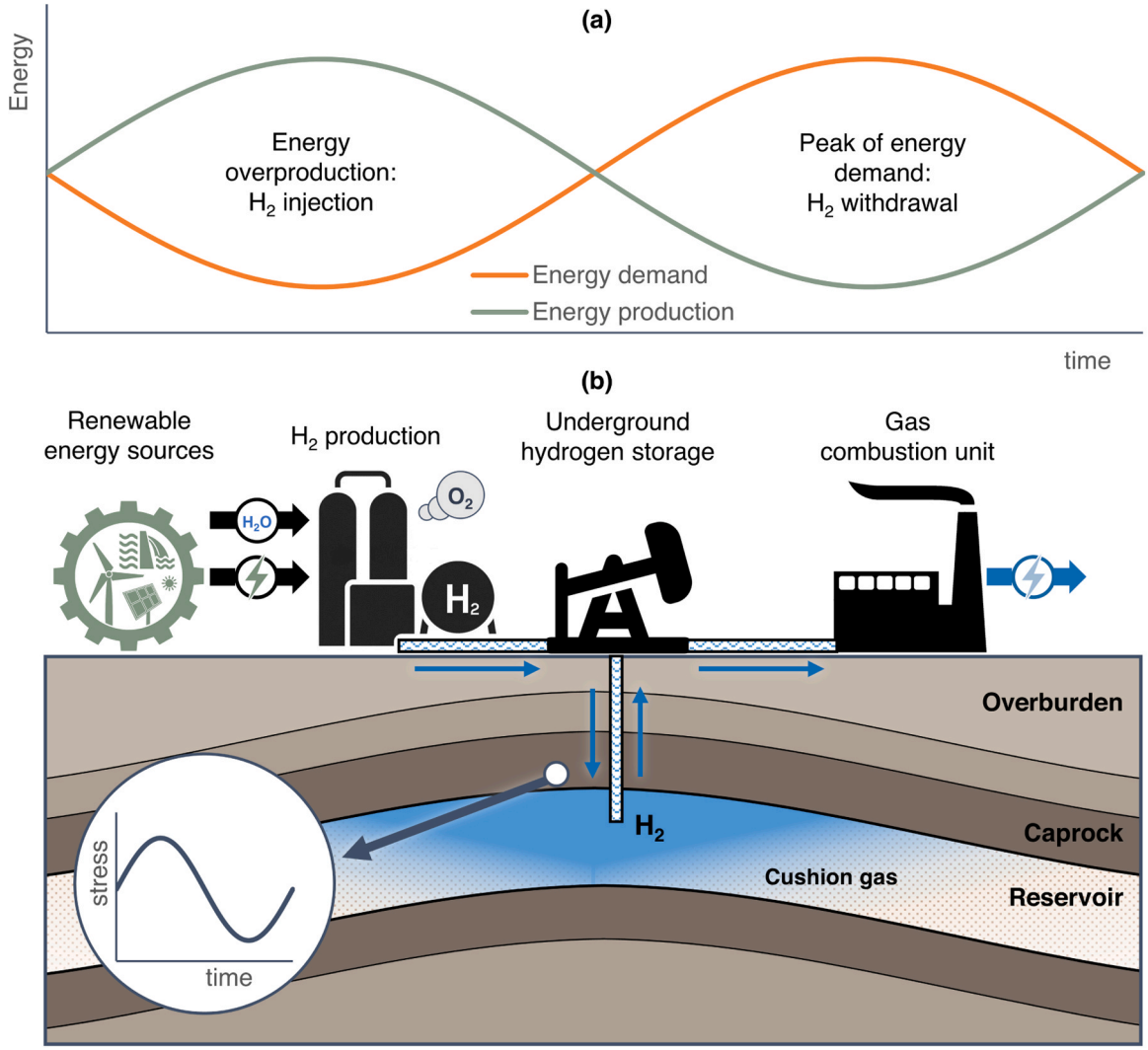

Fig. 1. (a) Renewable energy production/demand balance; (b) hydrogen injection/production operations in depleted oil and gas reservoir (inspired by [3]).

abandoned wells might constitute a possible way of preferential leakage so they have to be adequately sealed.[21] The effect of stress changes in the reservoir may indeed affect wellbore stability during hydrocarbon production,[22] moreover the chemical interaction between the well and the gas may induce corrosion and mechanical degradation of the completion.[23] Furthermore, caprock integrity studies need to be carried out, as pore pressure depletion during the previous production phase of the reservoir may have brought the stress state in the flanks of the overburden relatively close to failure conditions.[24]

Fig. 1 shows a schematic representation of the storage operations of hydrogen (produced by electrolysis) in depleted oil and gas reservoirs because of the balance between energy production and energy demand on an annual scale. Further details and similar illustrations can be found in Heinemann et al.[3].

The concept of underground gas storage has been already successfully applied to store natural gas as well as for carbon capture purposes (e.g., [25]). Therefore, in principle, it should be easy to apply the same idea to hydrogen storage by taking advantage of the large experience gained with the several underground gas storage facilities active worldwide. Nevertheless, a limited number of pilot studies have been conducted on underground hydrogen regulation, mainly involving storage operations for town gas, namely gas mixture with a certain percentage of hydrogen (e.g., [17,19]). The reason for this lies in the peculiar physical and chemical properties of hydrogen which pose a wide range of scientific challenges, as highlighted by several recent studies.[3,14-16]

Firstly, its low viscosity and high diffusivity increase the risk of leakage through the caprock and lateral trap structures and the likelihood of viscous fingering.[14] The complex multiphase interaction between hydrogen and in situ pore fluids can lead to contamination of stored hydrogen through the production of other gases.[3] Such geochemical interactions can also cause partial dissolution or precipitation of both reservoir and caprock minerals, in turn affecting their mechanical and hydraulic properties. In addition, the presence of hydrogen within the porous formation can increase microbial activity, which enhances the methanogenic process, converting hydrogen to methane and leading to hydrogen losses.[26,27]

Besides the geochemical interaction with the in situ materials, underground gas storage also involves a mechanical interaction induced by the injection-production processes, leading to changes in the effective stress state not only in the reservoir material but also in the overlying caprock. For example, the mechanical effects of hydrocarbon production have been extensively studied in reservoir geomechanics. The reduction in reservoir pore pressure causes material compaction, leading to surface subsidence and variations in the caprock stress state (e.g., [28-30,31]). Conversely, the mechanical effect of gas injection implies a progressive expansion of the reservoir material, which may lead to an increase in the deviatoric stress acting on the overburden caprock, as analysed in the context of carbon capture and storage studies.[32] While the above scenarios typically result in a monotonic variation of the stress state within the caprock, the alternation of hydrogen injection and production will induce a cyclic loading characterized by a strain rate associated with the seasonality of renewable energy sources (Fig. 1b). Indeed, the caprock will experience a complex cyclic stress path driven by the reservoir deformations. The latter may eventually result in progressive degradation of the material properties, potentially easing the development of leakage pathways that may compromise the integrity of the formation.[3] Similar stress paths may be also applied in subsurface reservoirs due to temporary storage of natural gas (e.g., [33,34,35]). For example, Jeanne et al. [36] numerically investigated the influence of natural gas injection/withdrawal sequences on the response of the Honor Rancho underground storage facility in Los Angeles County, showing that plastic reservoir compaction can induce irreversible deformations in the caprock material that may compromise its sealing integrity.

The influence of cyclic loading due to underground hydrogen storage has already been recognized in feasibility studies related to salt rock caverns, both from an experimental and a numerical point of view.[37-40] However, to the best of our knowledge, there is no experimental evidence in the literature regarding the impact of fatigue on the response of caprock materials of oil and gas reservoirs, which in many cases might either be shales or structured stiff clays subjected to large confining pressures.

This paper presents the preliminary results of an ongoing experimental investigation of the monotonic and cyclic response of caprock materials. The research aims to highlight the distinctive features of material behaviour under cyclic loading in order to develop an effective methodology for an early assessment of eventual fatigue-related risks in underground hydrogen storage projects involving clayey caprocks. Although the research focuses on underground hydrogen storage, the results are of general interest when dealing with cyclic subsurface fluid/gas storage.

The tests were performed on undisturbed samples representative of a typical overburden caprock of hydrocarbon reservoirs. The basic material properties are firstly presented together with a definition of the initial state of the samples in terms of in situ stress and sample suction. The latter, together with the comparison between laboratory and in situ elastic wave velocities, is used to provide a preliminary check on the quality and representativeness of the undisturbed samples, which is particularly relevant given the importance of material structure to its mechanical response. The results of consolidated undrained triaxial tests are then shown to analyze the stress-strain behaviour of the structured clay under monotonic and cyclic loading. Particular emphasis is placed on the analysis of the effect of strain rate on the mechanical response. Finally, the results of the cyclic triaxial test are presented to show the progressive material destructuration under fatigue loading until failure. Cyclic degradation is also discussed in terms of variation in elastic wave velocities of the specimen monitored during the triaxial test.

2. Material characterization

The material under consideration is a plio-pleistocenic structured Italian clay. The mechanical behaviour under monotonic loads of similar materials has been studied in many previous works (see e.g., [41,42]), however in such cases the samples were proceeding from shallow depths. In the present study, undisturbed samples were cored from a deep formation above a hydrocarbon reservoir, known as "Argille del Santerno" ("Santerno Clay") at a depth of about 1150 m. Although such reservoir is not currently being considered for hydrogen storage, the study was conducted on this material because of the availability of high quality samples retrieved from a formation with a geological history and physical properties that are quite common for underground gas storage projects. In geotechnical engineering, materials from this and similar formations are usually defined as stiff clays (e.g., [43,44,41,42]), and this is the terminology that will be adopted throughout this paper. However, it is worth noting that the same materials are usually referred to as shales in the oil and gas engineering literature (e.g., [45]).

The adopted coring system was designed to maintain the original petrophysical and mechanical characteristics of the formation. It was made with a hydrolift-type total closure system, aluminum inner barrels 4 ¾" x 4 ¼" (Outer Diameter x Inner Diameter) x 32 feet' with a pressure relief valve suitable for preventing possible damage in the event of undesired gas expansion during extraction. The core bit was of the face discharge type, for soft or moderately consolidated formations. This ensured minimum contact between the drilling mud and the core. Also, the core head was a low invasion PCD (Poly-Crystalline Diamond) type for soft or moderately consolidated formations. After coring, the cores were immediately stabilized by sealing them with foam, and carefully handled to the laboratory, where samples to be tested were subcored.

In the following sections, the results of the preliminary and mineralogical characterization are reported together with the determinations of the suction of the samples as delivered to the laboratory and of the water retention properties. The latter were used to assess the quality of the samples, along with a comparison between laboratory and in situ

elastic wave propagation velocities.

2.1. Index properties and mineralogy

A series of tests including grain size distribution, Atterberg limits, and X-ray analysis were performed to determine the index properties and mineralogy of the soil. The grain size distribution (Fig. 2) showed that the clay fraction is 49.6%, silt is 49.5% and sand is 0.9%.

Table 1 summarizes the average value of clay minerals, carbonate, and silicate contents of several samples from the same core. The X-ray diffraction revealed that clay minerals constitute about 36.3% of the solid phase, illite and kaolinite being the dominant ones with percentages of 26.2% and 6.3%. Minerals of the carbonate family are very abundant, with a calcite fraction of 28.1% and a dolomite one of 10.7%.

The specific gravity was found to be $G_S = 2.78$. The liquid limit determined with distilled water is $w_L = 43.49\%$ whereas the plastic limit is $w_P = 25.34\%$ (plasticity index $PI = 18.15\%$).

2.2. Initial state

Cylindrical specimens with a diameter 10 mm and height of 10 mm were sub-cored from the undisturbed samples to characterize their initial state. Specimens were oven dried at 110 °C for 24 h for the determination of the natural water content, which was found to vary between $w = 12.8\%$ and $w = 14.3\%$. Accordingly, the consistency index CI of the specimens varied between 1.61 and 1.69. The void ratio e of the specimens varied between 0.37 and 0.42, so that an initial degree of saturation S_r^i was found to vary between 0.92 and 0.98.

The vertical total stress at the depth of recovery was determined from the integration of density logs and it was found to be $S_v = 25.90$ MPa. The in situ pore pressure was reconstructed from direct borehole measurements (taken at the most permeable soil layers) together with analysis of log data at the depth of interest (mainly sonic and density data) by identifying normal compaction trend lines through mathematical regression (see also [46,47]). The final value resulted to be $p_w = 13.62$ MPa, whereas from leak-off tests and break-out analyses[48] the stress components in the horizontal plane were expected to be isotropic ranging between $S_{h,1} = 19$ MPa and $S_{h,2} = 20$ MPa.

A preliminary check on the sample quality/conservation was obtained by comparing the sample suction with the one theoretically induced by an ideal coring operation. Assuming an elastic unloading process, undisturbed coring leads to the following estimate of capillary pressure:

$$s = u_a - u_w = -(p_w - Bp_0) \quad (1)$$

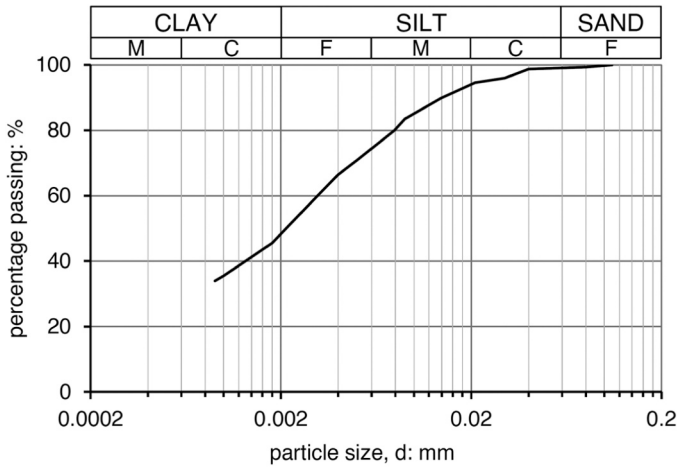

Fig. 2. Grain size distribution of the material.

Table 1
Mineralogy of the tested material.

Carbonates, silicates, and clay minerals	Average content (%)
Calcite	28.1
Dolomite	10.7
Quartz	15.4
Plagioclase	7.3
Illite	26.2
Kaolinite	6.3
Chlorite	3.8
Others	2.2

where: u_a is the air pressure; u_w is the water pressure at the back of the meniscus; B is Skempton's[49] pore pressure parameter; and p_w and p_0 are the in situ pore pressure and mean total stress, respectively. Conservatively assuming $B = 1$, it follows an expected matric suction due to undisturbed coring $s \cong 7.68 \div 8.64$ MPa.

The filter paper technique (ASTM D5298–16[50], see also [51]) was used to measure the total suction ψ and the matric suction of the delivered samples by using sheets of Schleicher and Schuell No. 589 filter paper. The calibration line in ASTM D5298–16[50] was adopted, determining a matric suction $s = 6.59$ MPa and a total suction $\psi = 9.35$ MPa from which an osmotic suction $\pi = 2.76$ MPa, results. The total suction was also determined using a DECAGON WP4 chilled mirror psychrometer (ASTM D6836–16[52]) and a value of 8 MPa was obtained in this case. The matric suction experimentally determined is smaller than the one predicted with Eq. (1). Accordingly with Doran et al.[53], the theoretical suction depends on the possible anisotropy of the material stiffness, and it is smaller than the one of the isotropic case when the horizontal stiffness is smaller than the vertical one.

2.3. Representativeness of the samples

The water retention behaviour was investigated with the vapor equilibrium technique. Small specimens were cut from the undisturbed samples and placed in sealed containers, whose air relative humidity was controlled by partially filling them with saturated saline solutions.[54] Five salts were used to such an extent. The total suction imparted with the saline solutions was double-checked with the WP4, obtaining the values presented in Table 2.

The specimens were weighted every day until a constant mass in time was observed. The gravimetric water content at equilibrium for each suction was used to determine the water retention curve shown in Fig. 3, where it is compared with the measurement of the initial conditions of the samples.

The initial state of the samples plots slightly above the water retention measurements, suggesting that a small hysteretic wetting occurred for the sample exposed to the lower suction, while the other determinations appear to belong the main drying curve. These results indicate that a limited drying occurred during sample storage. However, the very high degrees of saturation and the fact that initial suction compares reasonably well with the one predicted theoretically, suggest that the quality of the samples is high, and no significant alteration has occurred in their fabric during the coring and storage stages.

These observations are also confirmed by the comparison, shown in Fig. 4, between P- and S-wave velocities at small strains, V_P and V_S,

Table 2
Salts used to obtain the water retention curve.

Saturated salt solution	Measured total suction ψ (MPa)
K2SO4	5.08
BaCl2·2H2O	14.27
KCl	22.72
NaCl	38.73
NaNO2	59.10
CaCl2·6H2O	159.09

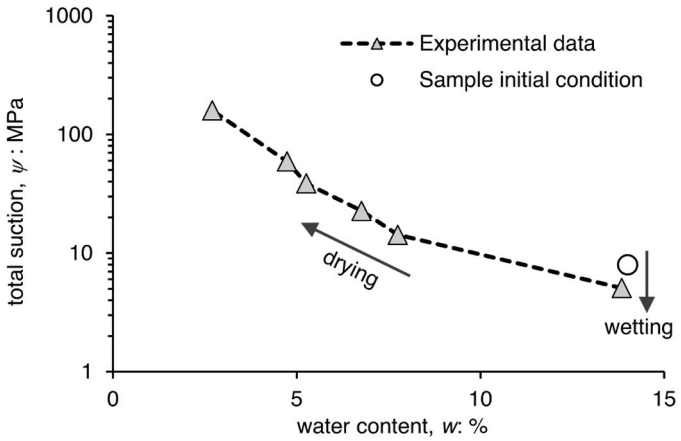

Fig. 3. Water retention determinations.

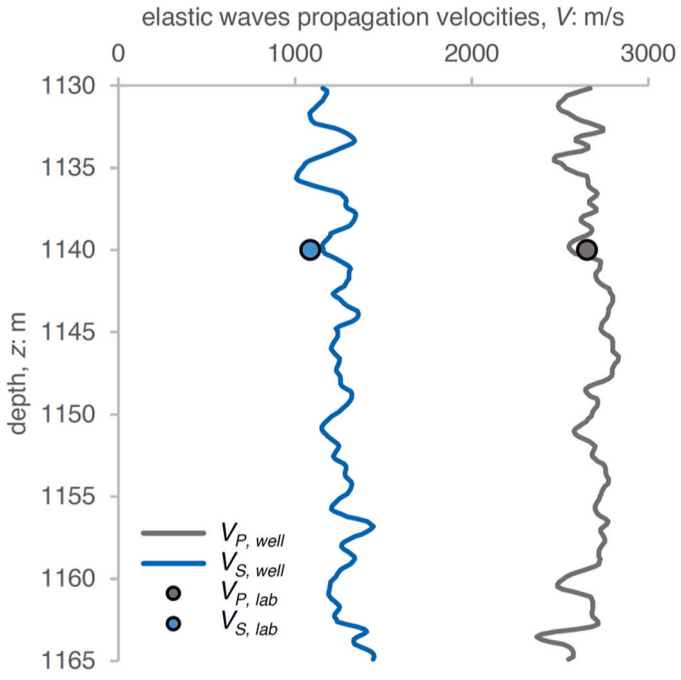

Fig. 4. Comparison between laboratory P- and S-wave velocities with wellbore sonic logs.

measured in situ and in the laboratory. The continuous measurement of $V_{P,well}$ and $V_{S,well}$ was obtained by sonic logs conducted within the caprock formation, in a well located approximately 150 m from the one from which the samples were taken. The elastic wave velocities characteristics of the cored samples, $V_{P,lab}$ and $V_{S,lab}$, were instead measured at the end of the consolidation stage of the cyclic triaxial test by means of acoustic velocity sensors (see Section 6).

For a given material state (in terms of stress state, degree of saturation, and porosity), an alteration of the structure, intended as both particle arrangement and bonds, may induce a decrease in elastic wave velocities. The joint analysis of laboratory wave velocities and wellbore sonic logs can therefore provide a quantitative evaluation of the representativeness of laboratory samples.[55]

As the samples and the log measurements are from two different wells, and no porosity logs are available, a precise quantitative evaluation of the structural representativeness, and therefore of the damage, of the collected samples such as in Musso et al.[55] is not possible. However, it can be observed that the compressive wave velocity measured in the experiments $V_{P,lab} = 2650$ m/s is very consistent with the average $V_{P,well}$ value, confirming not only the quality of the samples, but also the effectiveness of the saturation procedure carried out before the consolidation stage (see Section 3). A slightly lower $V_{S,lab} = 1088$ m/s is instead observed compared to the average $V_{S,well} \approx 1220$ m/s, which might suggest that the structure of the formation has been just slightly disturbed during coring and the samples can be considered representative of the in situ material response.

It is interesting to note that the results of the wave velocity measurements from the borehole sonic logs are in perfect agreement with the correlations proposed by Benetatos et al.[45] to estimate the expected in situ elastic moduli for some geological formations, including the "Argille del Santerno". Such relationships can indeed be used to give a rough preliminary estimate of the elastic wave velocities at the depth of interest, resulting in $V_{S,well} \approx 1250$ m/s and $V_{P,well} \approx 2650$ m/s.

3. Experimental procedures and testing programme

The triaxial tests were conducted on undisturbed samples in the medium- and the high-pressure triaxial apparatuses (MPTA and HPTA, respectively) of the geotechnical laboratory of the Politecnico di Torino, manufactured by GDS Instruments Ltd. and subsequently modified. A full description can be found in Barla et al. [56]. Cylindrical specimens with a height of 100 mm and a diameter of 50 mm were cored from intact samples and tested in the HPTA under monotonic conditions. The cyclic test was performed using the MPTA on a 76 mm high and 38 mm diameter specimen. The testing procedure encompassed the classical three stages of a triaxial test, namely: saturation, consolidation, and shearing.

The saturation phase deserves a detailed discussion. When preparing the apparatus, the specimens are set using the dry setting method, which avoids undesirable swelling that could affect the structure of the material.[57] However, this technique prevents obtaining an initially fully saturated apparatus as it regards pore pressure pipes and porous stones. An additional stage of flushing is then carried out by applying a pore pressure gradient (about 60 kPa) between the bottom and top faces. As a result, deaerated water passes through the entire equipment hydraulic system, removing most of the trapped air. It is worth noting that the water flows around the sides of the sample rather than through it, as some strips of filter paper are applied to the sides of the sample. This phase is usually carried out under an effective confining stress (in this case approximately 250 kPa) such as to avoid excessive swelling (the limit was set to a maximum negative volumetric strain $\varepsilon_v = -1\%$), the latter being monitored by local axial and radial transducers. In previous experimental studies carried out on similar materials, the above procedure has proved effective in achieving an acceptable initial degree of saturation of the specimen and apparatus ensemble, while avoiding excessive disturbance to the material structure.[58-60]

Subsequently, a typical backpressure procedure is employed to saturate the specimen. The cell pressure is increased under undrained conditions and the Skempton's[49] B-parameter is computed as the ratio between the measured pore pressure increase Δu_w against the applied $\Delta\sigma_c$. If the B value is greater than 0.95, the saturation phase is assumed to be complete. Otherwise, the drain is reopened while keeping the effective pressure constant (thus increasing the imposed backpressure) and the step is repeated after a certain time. The increase in backpressure implies an increase in the solubility of air in water according to Henry's Law and therefore a higher degree of saturation. It should be noted that the B-value can be strongly influenced by the system compressibility, especially in the case of stiff soils.[61,62] Although specimens cored from undisturbed sample showed an average initial degree of saturation $S_r^i = 0.93 - 0.96$, relatively low B values were observed initially due to the apparatus not being fully saturated. However, the coefficient increased rapidly with increasing backpressure u_w, reaching values greater than 0.95 for u_w of about 4 MPa. Some further B-checks

have shown that the B-value exceeded 0.97 at the end of the subsequent consolidation phase.

After saturation, the specimens were anisotropically consolidated under K_0 conditions up to an effective stress state consistent with the expected lithostatic one, namely: $p_0' = 8.1$ MPa and $q_0 = 6.3$ MPa. The axial stress rate $\dot{\sigma}_{ax}$ applied during the consolidation stage was defined on the basis of Terzaghi's one-dimensional consolidation equation for the case of a vertical load that increases linearly with time (see e.g., [63]). In this case, the excess pore pressure at the base of the consolidating layer $u_{w,b}$ tends to a constant value provided by the expression:

$$u_{w,b} = \frac{H_d}{2 \cdot c_v} \dot{\sigma}_{ax} \tag{2}$$

where H_d is the height of the drainage layer and c_v is the coefficient of vertical consolidation, which in the stress range of interest was determined to vary between $2 \cdot 10^{-7}$ and 10^{-6} m^2/s through oedometer tests conducted on the undisturbed material. Through Eq. (2), where c_v was assumed equal to $2 \cdot 10^{-7}$ m^2/s and $u_{w,b}$ was imposed to be 0.2 MPa, (i.e. 2.5% of p_0'), the $\dot{\sigma}_{ax}$ was determined to be 0.12 MPa/h and 0.2 MPa/h, for 100 mm and 76 mm high specimens respectively. These $\dot{\sigma}_{ax}$ values correspond to total consolidation times of approximately 100 h and 66 h. Similar to the time to failure at shearing, such values can be further decreased due to the presence of the lateral filter strips, which shorten the drainage length.[64] The final assumed consolidation times are set at 72 h and 48 h, for 100 mm and 76 mm high specimens respectively. These times were sufficient to achieve a fully drained consolidation phase, as indicated by the variation of backvolume over time, which showed a practically flat trend at the end of the consolidation.

The final stage consisted of shearing the specimens under undrained conditions. Three specimens were monotonically sheared under strain control using constant axial strain rates $\dot{\epsilon}_{ax}$ equal to 0.0005%/min, 0.01%/min, and 0.5%/min, respectively. The intermediate value was computed according to the ASTM D4767–11[65] standard. The larger $\dot{\epsilon}_{ax}$ is instead consistent with the average value implicitly adopted during the cyclic triaxial test, which is conducted by imposing a cyclic stress history to the specimen all the way up to failure. In the latter test, the deviator q was firstly increased under undrained conditions up to $q_{mean} = 9.75$ MPa. Subsequently, a sinusoidal loading was applied around q_{mean} with an amplitude $A = 3.25$ MPa and a corresponding maximum deviator $q_{max} = 13$ MPa. Such an amplitude value was selected by referring to real data from gas storage fields from Northern Italy, where the pore pressure amplitude in the reservoir material was found to be in the range between 3 and 6.5 MPa.[34]

The cyclic test was carried out using the MPTA, which was recently instrumented with acoustic velocity transducers (manufactured by GDS Instruments) embedded in the top cap and the pedestal of the triaxial cell. Each sensor package contains P-wave and S-wave elements able to receive and transmit. The input motions are typically pulses with a duration of 1 μs, characterized by a central frequency of about 1 MHz and applied towards either the positive or the negative verse. During the cyclic shearing, the signals are acquired at the end of each cycle for a scan time of 500 μs, adopting a sample time of $8 \bullet 10^{-3}$ μs.

4. Monotonic behaviour and strain rate effects

The results of the tests are presented in Fig. 5 in terms of stress-strain $q - \epsilon_{ax}$ responses and excess pore water pressure Δu_w build-up. The comparison between the tests shows the dependency of the mechanical response of the material on the axial strain rate $\dot{\epsilon}_{ax}$. The behaviour is particularly fragile for the three monotonic tests, showing a marked softening from ϵ_{ax} of 0.01–0.025 (respectively for shearing conducted adopting $\dot{\epsilon}_{ax}$ ranging from 0.0005%/min to 0.5%/min, see Fig. 5a), as expected for very stiff clays with a significant percentage of carbonates.

As regards the volumetric response of the material, positive Δu_w are initially accumulated by the specimens up to q_f. Thereafter, Δu_w tends to

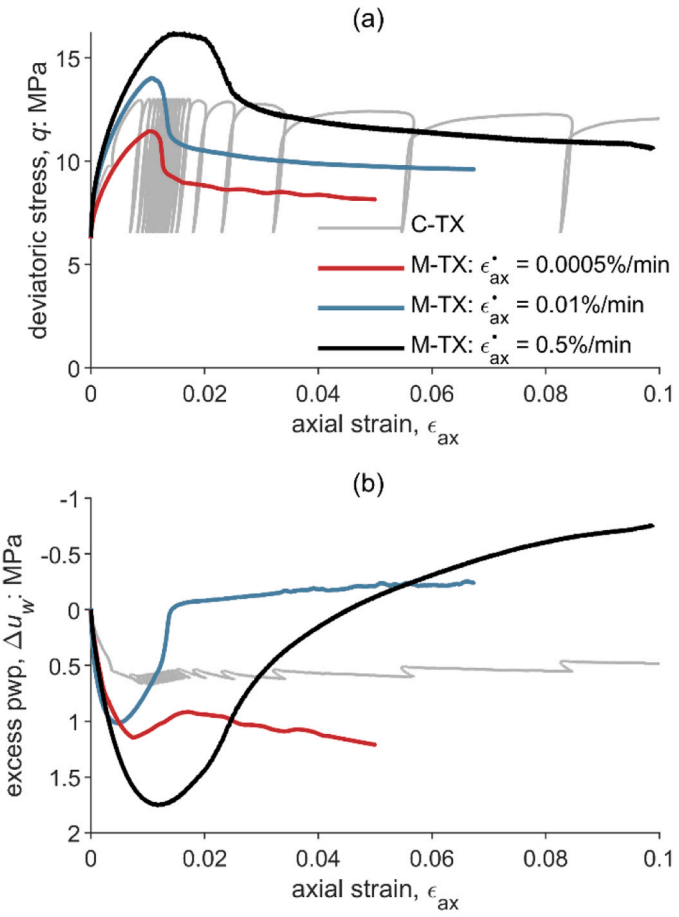

Fig. 5. Results of the anisotropically consolidated ($p_0' = 8.1$ MPa, $q_0 = 6.3$ MPa) undrained triaxial tests in terms of (a) deviatoric stress q and (b) excess pore-water-pressure Δu_w versus axial strain ϵ_{ax}.

rapidly decrease at the onset of the brittle failure, approaching zero while moving towards the post-failure resistance at large ϵ_{ax} (Fig. 5b). Such a slightly dilatant response is characteristic of the behaviour of structured clays and it is usually associated with the progressive development of the shear band within the specimen starting at peak strength.[44] The latter can be visualized in Fig. 6, which shows the typical single well-defined slip surface observed in the specimens after either monotonic or cyclic failure. Once the development of the rupture surface is completed, the subsequent post-failure accumulation of ϵ_{ax} occurs as a practically rigid-body sliding of the two parts of the specimen along the slip plane.

The influence of $\dot{\epsilon}_{ax}$ on the peak strength of the material is quite obvious also from the stress paths presented in Fig. 7. In the plot, the strain-controlled triaxial tests of this study are also compared to the peak failure envelope (orange dashed line) obtained from several stress-controlled monotonic tests (scatter points in Fig. 7) previously carried out. The latter tests were conducted adopting a deviator stress rate $\dot{q} = 300$ kPa/min. The resulting $\dot{\epsilon}_{ax}$, averaged along the whole failure stage, were approximately mid-range of the values used in the strain-controlled tests. As consequence, the failure envelope lies between the peak strengths observed in the triaxial tests.

The strain rate dependency of the strength envelope and, thus, of the yield surface is well known from the literature and it can be explained assuming an influence of $\dot{\epsilon}_{ax}$ on the preconsolidation pressure of the material. An in-depth discussion about strain rate effects can be found in Augustesen et al.[66]. The shaded zone depicted in Fig. 7 is a qualitative representation of the area comprising the strength envelopes of specimens sheared with $\dot{\epsilon}_{ax}$ ranging from 0.01 to 0.5%/min. The dashed black

Fig. 6. Typical single well-defined slip surface forming at failure in either monotonic or cyclic triaxial tests.

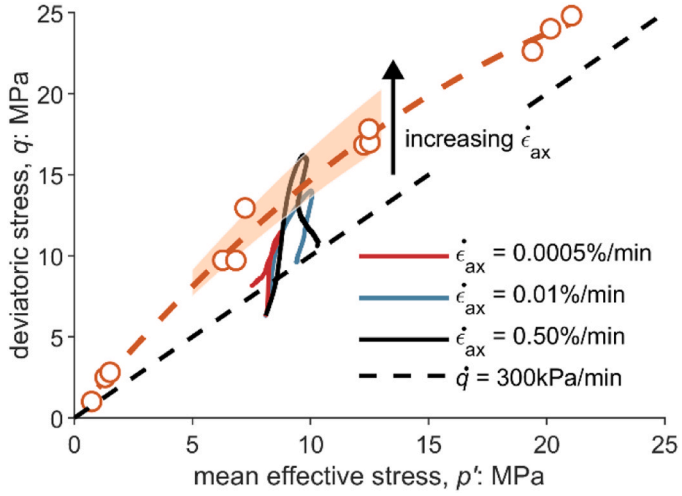

Fig. 7. Effective stress paths obtained from monotonic tests conducted at different strain rates $\dot{\epsilon}_{ax}$ compared to the peak failure envelope defined based on stress-controlled tests. The shaded area represents the qualitative failure envelopes for $\dot{\epsilon}_{ax}$ ranging from 0.01 to 0.5%/min. The dashed black line, corresponding to $q/p' = 1$, represents an estimation of the stress obliquity after failure.

line corresponds to $q/p' = 1$, which is thought to be a reasonable estimation of the stress obliquity after failure. The stress paths tend to the same final value of the stress ratio q/p' for both the tests, suggesting that the $\dot{\epsilon}_{ax}$ does not influence the residual strength of the specimen. It can be observed that the commented stress paths of the undrained tests bend to the right since the beginning, which together with the suction measurements commented in Section 2.2 suggests that the vertical stiffness might be higher than the horizontal one.

5. Cyclic response

The results of the cyclic test are compared to the monotonic curves in Fig. 5. The specimen shows a progressive accumulation of ϵ_{ax} with increasing loading cycles (Fig. 5a). The cyclic loading history was characterized by a period $T = 5$ min (i.e., frequency $f = 0.0033$ Hz). While the actual axial strain rate increased in the last cycles of the test, the average strain rate $\bar{\dot{\epsilon}}_{ax,c}$ can be computed as:

$$\bar{\dot{\epsilon}}_{ax,c} = \frac{4\bar{\epsilon}_{ax,c}}{T} \tag{3}$$

being $\bar{\epsilon}_{ax,c}$ the average axial strain applied during a quarter of the cyclic loading. The resulting $\bar{\dot{\epsilon}}_{ax,c} = 0.22\%$/min is consistent, at least in terms of order of magnitude, with the faster monotonic test ($\dot{\epsilon}_{ax} = 0.5\%$/min). The response is quite stable during the first loading cycles, whereas it rapidly degrades for ϵ_{ax} larger than about 0.02 all the way up to failure. It is then interesting to notice that the cyclic $q - \epsilon_{ax}$ curve obtained under stress-control is well enveloped by the monotonic response measured at the higher strain rate, while it extends outside of the monotonic response measured at the other two strain rates (namely $\dot{\epsilon}_{ax} = 0.01\%$/min and 0.0005%/min).

As concerns the pore pressure build-up, Δu_w initially increases with ϵ_{ax}, consistently with the monotonic behaviour (Fig. 5b). On the contrary, the cyclic response does not show the abrupt decrease of Δu_w occurring in the monotonic tests at the onset of the slip surface. A possible explanation for such a difference is that during a stress-controlled cyclic test the actual $\dot{\epsilon}_{ax}$ is much larger when approaching failure than the average $\bar{\dot{\epsilon}}_{ax,c}$ value. Consequently, the response of the specimen during the last cycles is governed by a failure envelope that is, likely, even above the one obtained for $\dot{\epsilon}_{ax} = 0.5\%$/min. This would in turn correspond to less pronounced Δu_w dissipation with increasing ϵ_{ax} despite the shear band is developing throughout the specimen.

The accumulation of permanent strains during cyclic loading yields to the development of the rupture surface (Fig. 6) and, in turn, the progressive reduction of the specimen strength. The test keeps going on as far as the resistance is still larger than the maximum applied deviator, namely $q_{max} = 13$ MPa. When the load approaches the strength of the specimen (reduced from its initial, peak, value) failure occurs under loading control. Cyclic failure therefore takes place as a result of the degradation of the material structure.

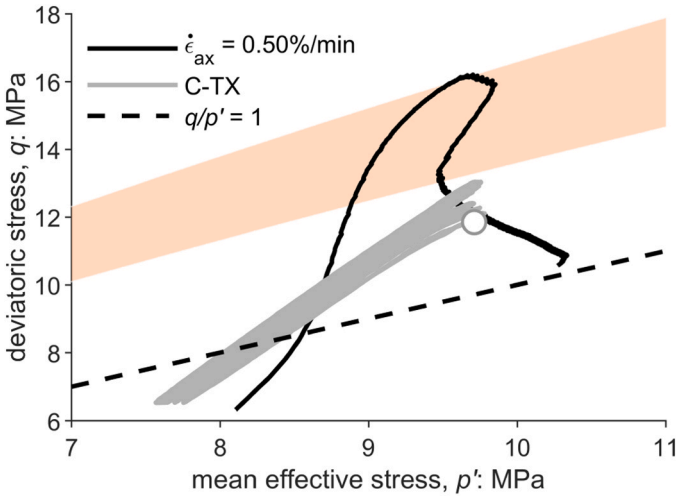

Fig. 8. Effective stress paths of monotonic and cyclic triaxial tests performed at a consistent $\dot{\epsilon}_{ax}$. The shaded area represents the qualitative failure envelopes for $\dot{\epsilon}_{ax}$ ranging from 0.01 to 0.5%/min.

Such interpretation is also confirmed by the cyclic stress path represented in Fig. 8. The stress path is below the shaded area qualitatively identified as the failure zone for $\dot{\epsilon}_{ax}$ between 0.01% and 0.5%/min. As it can be observed, the cyclic failure (represented by the empty circle) takes place well-below the peak resistance identified by the corresponding monotonic test. The cyclic stress ratio q/p' at failure is thus somewhere between the initial peak strength and the residual value equal to about 1.

The results of the test can be analyzed in light of synthetic cyclic parameters, defined in Fig. 9 for a typical stress-strain loop. Specifically, the mean axial strain $\epsilon_{ax,m}$ is defined as the ϵ_{ax} at the end of each loading cycle, while the cyclic axial strain $\epsilon_{ax,c}$ is equal to half-amplitude of the strain loop. The evolution of the material stiffness is analyzed with reference to the secant loading Young's modulus measured during the first quarter of the cycle E_l and to the unloading modulus E_u. Equivalently, it is possible to define the correspondent secant shear moduli G_l and G_u assuming null volumetric strains (as usual under undrained conditions). Note that these parameters do not necessarily refer to elastic properties, but to secant values averaged over the specimen size.

The variation of the abovementioned parameters with the corresponding loading cycle N is presented in Fig. 10a-c. In addition, Fig. 10d presents the total strain energy W_{tot} supplied to the specimen for a given number of loading cycles N, computed as:

$$W_{tot} = \int_0^{\epsilon_S(N)} q \cdot d\epsilon_S \tag{4}$$

where ϵ_S is the deviatoric strain, equal to ϵ_{ax} under the hypothesis of null volumetric strains.

The $\epsilon_{ax,m} - N$ evolution (Fig. 10a) exhibits an initial, faster, increase during the first loading cycles followed by a progressive stabilization characterized by an almost constant rising trend until the 13th cycle. The onset of the brittle failure causes afterwards a sudden accumulation of permanent strains. Consistently, the cyclic axial strain $\epsilon_{ax,c}$ is practically constant, and equal to 0.001, from the 2nd to the 13th cycle, while it shows an almost twenty-fold increase (up to about 0.017) in the last cycles (Fig. 10b). Such a behaviour can be explained by observing the G_l and G_u trends depicted in Fig. 10c. G_l initially increases up to about 670 MPa due to the progressive stabilization of the material response which leads also to a slow accumulation of permanent strains during the first 13 cycles. After the 13th cycle, the progressive development of the failure surface within the specimen induces a dramatic decrease of G_l.

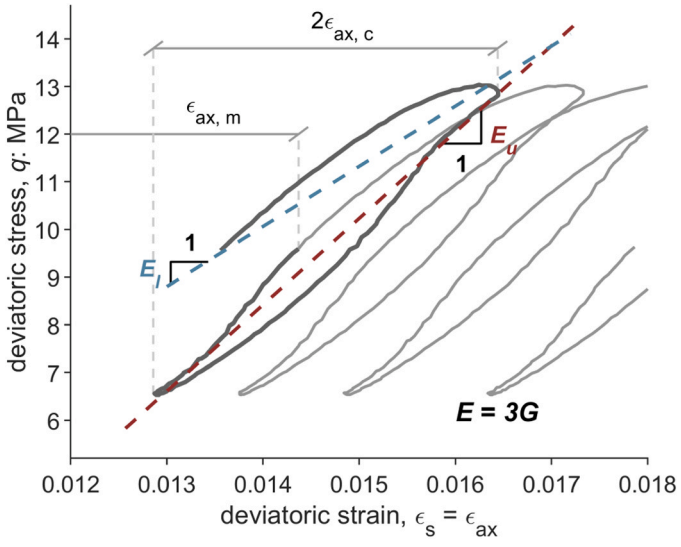

Fig. 9. Definition of the parameters adopted to describe the undrained stress-strain loops.

On the other side, the unloading modulus G_u is not substantially influenced by the cyclic loading, slightly decreasing from 950 to 850 MPa.

In a cyclic triaxial test performed under stress control, part of the strain energy supplied to the specimen is recovered during the unloading phase. As a consequence, the W_{tot} usually oscillates within a loading cycle (Fig. 10d). The remaining part of the energy is dissipated by the specimen due to the viscosity of the material (represented by the area enclosed within a stress-strain loop) and permanent strain accumulation. In the test here presented, the latter is particularly relevant for the 1st cycle and after the 13th one. As a result, a substantial increase of W_{tot} is observed during the last part of the test. In other words, this means that during the last cycles, when approaching failure, a much larger amount of energy has to be supplied to the specimen to apply the same cyclic stress history.

6. Analysis of elastic wave velocities

The degradation of the material structure with cyclic loadings leads to a progressive reduction of the secant shear moduli, as observed in Fig. 10. At the same time, it is reasonable to assume that such destructuration would also imply a decrease in the small-strain properties of the material, namely the shear (S) and compressional (P) wave propagation velocities V_S and V_P. As suggested by previous studies (e.g., [67]), these parameters may represent useful indicators for monitoring the response of materials subjected to fatigue loading. The V_S and V_P values were thus tracked during the cyclic triaxial test to define a reliable proxy for identifying the onset of the cyclic failure.

The propagation velocities were monitored during the cyclic test through acoustic velocity transducers. The first-arrival time t_0 for the reference scan x_0 (acquired at the end of the consolidation stage) was obtained by manually picking the received signals. Fig. 11 shows the reference signals for both P- and S-waves along with the identified first-arrival times.

A cross-correlation procedure was then implemented to define the variations in the arrival time $\Delta t(N)$ for the subsequent scans x_N acquired at the end of each N-th cycle. Specifically, the signal x_N is shifted according to several tentative time lags to identify the one which produces the best match with x_0. The selection criterion is based on the normalized cross-correlation coefficient $\rho(x_0, x_N)$, computed as:

$$\rho(x_0, \quad x_N) = \frac{R_{x_0,x_N}(\Delta t)}{\sqrt{R_{x_0,x_0}(0) \cdot R_{x_N,x_N}(0)}} \tag{5}$$

where $R_{a,b}(m)$ denotes the generic cross-correlation function between signals a and b, the latter being shifted by the tentative lag m. It is worth noting that the procedure is applied only to a portion of the signals, approximately centred on the first arrival time, in order to determine the time delay associated only with the direct wave propagating through the specimen.

The actual time lag $\Delta t(N)$ is defined as the value associated with the maximum normalized cross-correlation coefficient $\widehat{\rho}(x_0, x_N)$. When considering two signals totally equivalent in terms of shape and amplitude but shifted in time, $\widehat{\rho}(x_0, x_N)$ approaches 1 (as in the case of the autocorrelation function). However, generally speaking, x_0 and x_N differ due to experimental uncertainties and variations in the mechanical properties of the specimen. The coefficient $\widehat{\rho}(x_0, x_N)$ represents thus a measure of the similarity between scans taken at different instants of the test.

The arrival time is obtained as:

$$t(N) = t_0 + \Delta t(N) \tag{6}$$

Eqs. (5) and (6) are applied for either P- or S-wave signals, resulting in the corresponding maximum normalized cross-correlation coefficients $\widehat{\rho}_{P,S}(x_0, x_N)$ and arrival times $t_{P,S}$. Finally, V_P and V_S are computed as:

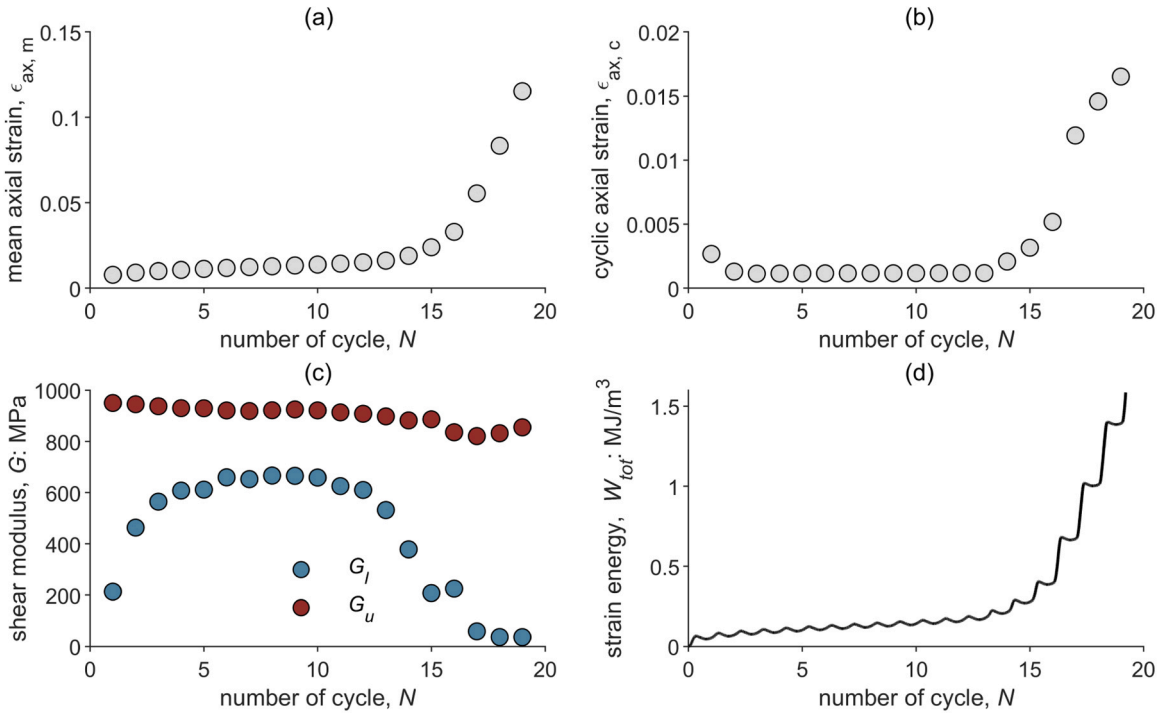

Fig. 10. Evolution of the material response with increasing loading cycles N in terms of: (a) mean axial strain $\epsilon_{ax,m}$; (b) cyclic axial strain $\epsilon_{ax,c}$; (c) loading G_l and unloading G_u cyclic shear stiffnesses; and (d) total strain energy W_{tot} supplied during undrained cyclic shearing.

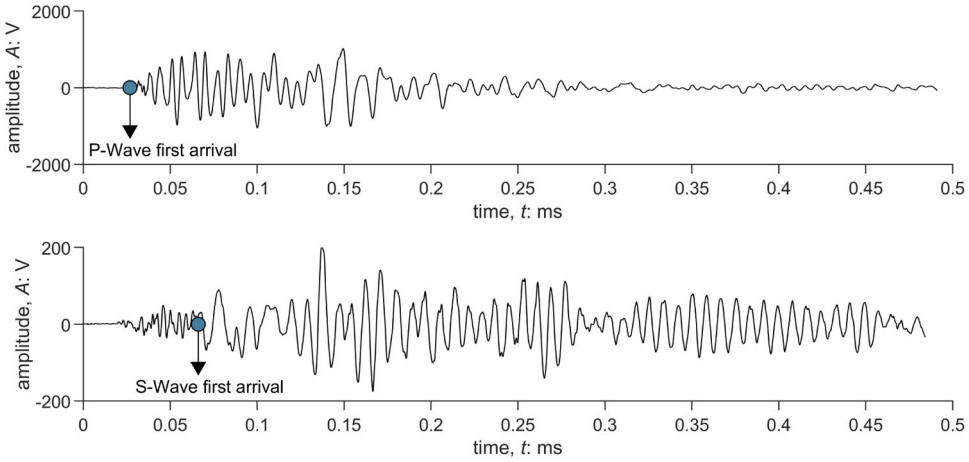

Fig. 11. Reference P- (top) and S- (bottom) wave signals acquired at the end of the consolidation stage. The scatter points show the identified first arrival times.

$$V_{P,S}(N) = \frac{H(N)}{t_{P,S}(N)} \tag{7}$$

where $H(N)$ is the current height of the sample.

Fig. 12 presents the comparison between the reference signals acquired before the shearing (black lines) and at the end of the 10th and the 19th cycle, the latter after being shifted in time through the cross-correlation procedure (Fig. 12a-b and Fig. 12c-d, respectively). In the plots, the dashed lines identify the time interval in which the cross-correlation procedure is applied.

The comparison shows the effectiveness of the processing technique, but also the differences between scans taken before and after the failure. The amplitude and the shape of the P-wave signals do not differ significantly from cycle to cycle (Fig. 12a-c). Conversely, larger differences are observed between S-wave scans taken at different stages (Fig. 12b-d). Such differences can be attributed to the development of the shear band within the sample.

The variation of V_P and V_S during the test is reported in Fig. 13a-b. An initial decrease of V_P and V_S can be observed in the first three cycles as a result of the initial pore pressure build-up (Fig. 7b). During the following cycles, however, both velocities tend to stabilize, showing just a slightly decreasing trend, in compliance with the evolution of the secant shear moduli shown in Fig. 10c. The failure surface starts to develop after the 13th cycle, leading to a decrease in the propagation velocities. Such a reduction is however less marked than the one observed in G_l and G_u (Fig. 10c). This can be explained by considering that the development of the shear band takes place in a quite narrow zone (Fig. 6). The thickness of the material layer interested by the mechanical degradation is indeed relatively small if compared to the whole size of the specimen. The influence of material destructuration on V_P and V_S is thus limited since the parameters reflect the propagation characteristics averaged over the specimen height.

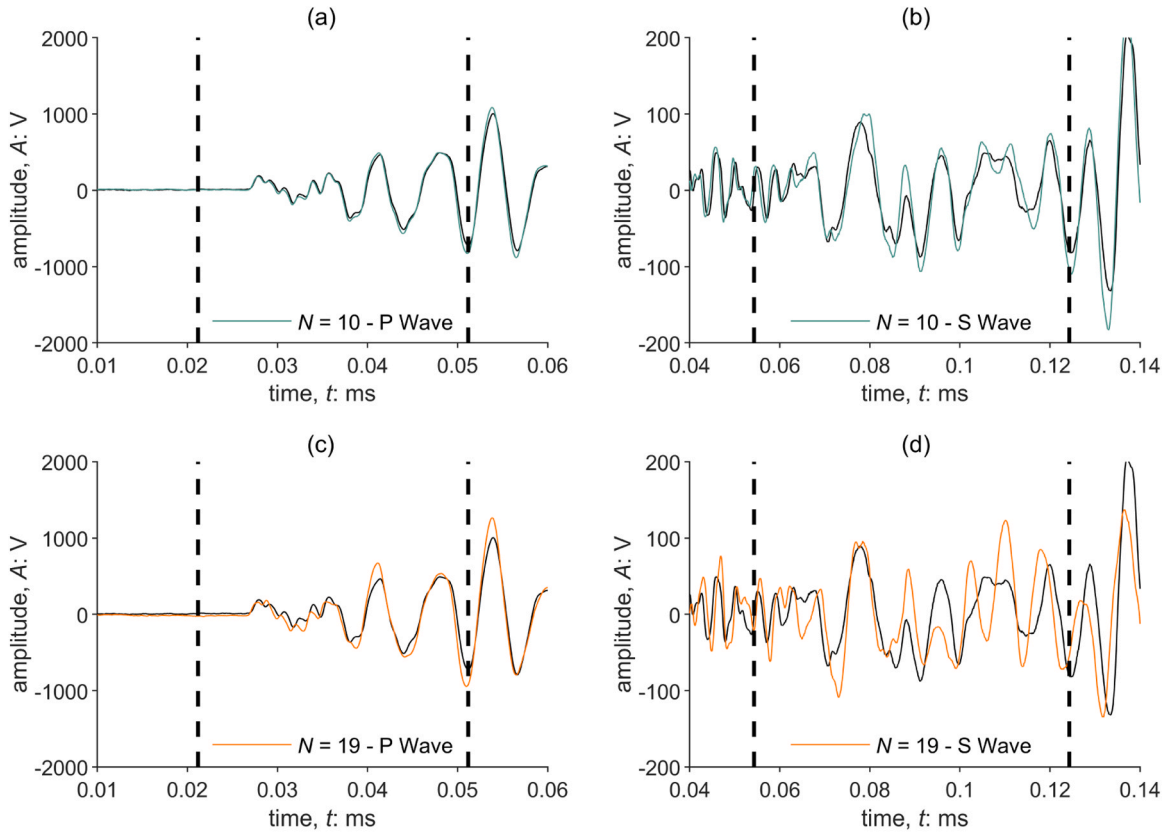

Fig. 12. Comparison between the reference signals acquired before shearing (black lines) and at the end of the 10th (green line) and the 19th (orange line) loading cycles for P- (a-c) and S- (b-d) waves, the latter after being shifted in time.

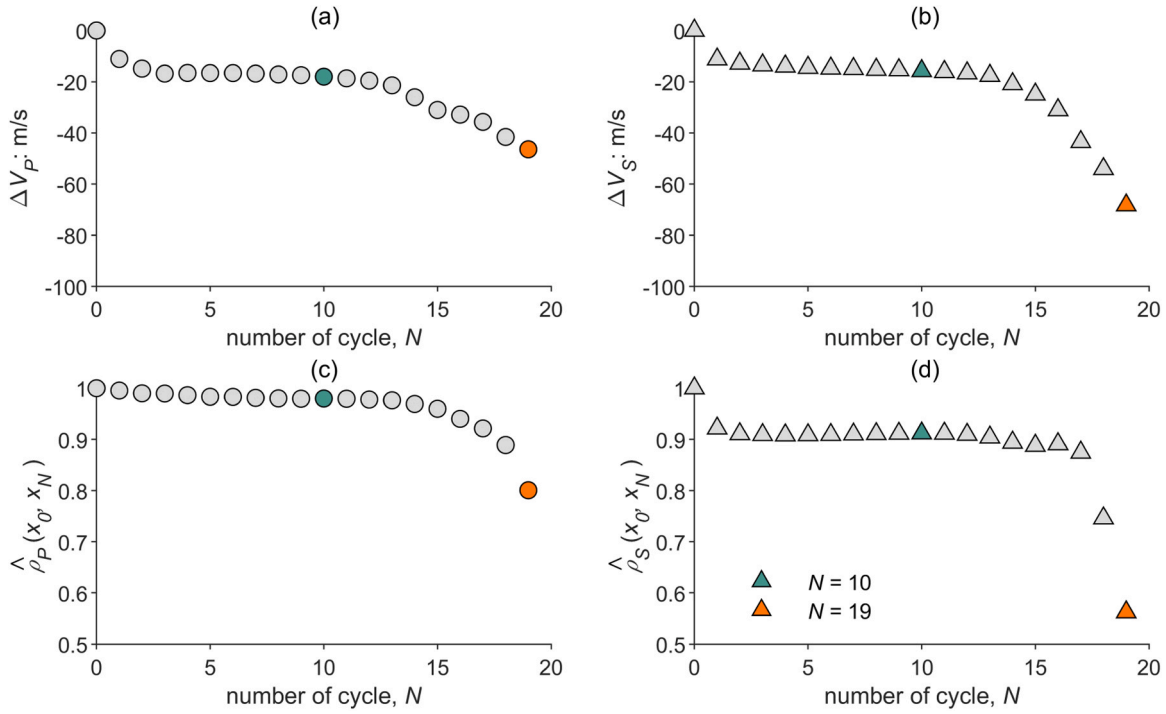

Fig. 13. (a-b) Variation of the compressional ΔV_P and shear ΔV_S wave velocities with increasing loading cycles N; (c-d) corresponding evolution of the maximum normalized cross-correlation coefficients $\widehat{\rho}_P(x_0, x_N)$ and $\widehat{\rho}_S(x_0, x_N)$.

Fig. 13c-d shows the variation of $\widehat{\rho}_P(x_0, x_N)$ and $\widehat{\rho}_S(x_0, x_N)$ with increasing loading cycles. In the plot, the points corresponding to the scans presented in Fig. 12 are highlighted. The results confirm the qualitative evidence of degradation previously discussed based on the visual inspection of the recorded signals. Indeed $\widehat{\rho}_P(x_0, x_N)$ assumes values approaching 1 (i.e., strong similarities among the signals) up to the 13th cycle. Conversely, $\widehat{\rho}_S(x_0, x_N)$ is on average equal to about 0.9, reflecting the larger aleatory variability which affects the estimation of V_S with respect to V_P. The development of the shear band significantly modifies the waves propagation phenomena within the specimen, leading to the generation of reflected and refracted waves which interfere with the direct wave. As a consequence, both $\widehat{\rho}_P(x_0, x_N)$ and $\widehat{\rho}_S(x_0, x_N)$ decrease, the latter being dramatically reduced down to about 0.5.

7. Discussion and conclusions

Depleted oil and gas reservoirs are expected to offer an effective long-term solution for underground hydrogen storage due to: (*i*) the large storage volumes available; (*ii*) the proven sealing ability of caprock formations to prevent gas migration; and (*iii*) the extensive information on caprock and reservoir materials already collected from hydrocarbon production operations. However, the use of hydrogen as an energy carrier still poses several scientific challenges related to the geochemical-mechanical interaction between the gas and the geological formations. From a strictly hydro-mechanical point of view, the injection-production operations lead to cyclic variations in the effective stress state of both the reservoir and the caprock material. From a theoretical point of view, such fatigue loading can cause progressive degradation of the caprock material, resulting in a reduction in shear strength and eventually the development of shear bands, the actual onset of which will depend on the material properties, in situ stress conditions, and production/injection rates specific to the case being analysed.

In this paper, the mechanical response of a stiff Italian clay has been preliminary investigated with the aim of highlighting peculiarities in the behaviour of caprock-like materials that may be relevant in the context of underground hydrogen storage. Laboratory tests were carried out on undisturbed samples taken from a deep caprock formation sealing a hydrocarbon reservoir. A preliminary material characterisation was carried out to assess the quality of the cored samples. Comparison of the water retention curve with the initial material suction suggests that no significant change in the sample fabric has occurred during coring and storage. This observation is further supported by the comparison of laboratory measured elastic wave velocities with borehole sonic logs, which showed a high degree of sample representativeness.

The monotonic and cyclic behaviour of the caprock material was analysed by means of undrained triaxial tests carried out on specimens consolidated to large confining pressures (namely: $p_0' = 8.1$ MPa and $q_0 = 6.3$ MPa), consistent with measured field values. The strain-controlled monotonic tests have shown that the mechanical response of the caprock is influenced by two peculiar aspects: (*i*) the material structure and (*ii*) the strain rate dependence. The stress-strain curves are characterised by a large undrained peak shear strength and marked post-peak softening. Such a fragile response is thought to be a consequence of the microstructure of the material, both in terms of the arrangement of the soil particles and the inter-particle bonding.[44] In addition, the mechanical behaviour of the material is significantly influenced by the strain rate during shearing. An increase in the strain rate implies indeed a larger peak shear strength. However, in agreement with previous experimental results obtained on clay specimens at lower confining pressures,[68-70] the residual strength does not appear to be affected by strain rate.

These two aspects observed under monotonic conditions, have also strong implications in the context of hydrogen storage operations. As shown by the stress controlled cyclic triaxial test, the application of fatigue loads induces an axial strain accumulation which results in a progressive degradation of the material structure. Eventually, a fragile cyclic failure occurs as the reduced material strength approaches the maximum applied deviator, as indicated by the comparison between the monotonic and cyclic responses. This result is consistent with previous experimental studies carried out mainly on rocks (e.g., [71,72,40,73]), which noted that the monotonic curve somehow envelops the cyclic stress-strain response of the specimen. For a clayey material characterised by a viscous response, this observation holds, provided that the monotonic behaviour is obtained at a strain rate corresponding to the average cyclic one. Something similar was observed experimentally by Lefebvre & LeBoeuf [68] based on the results of cyclic triaxial tests carried out on sensitive clays from shallow depths. However, to our knowledge there are no reported experimental results on the strain rate dependence of the cyclic behaviour of structured stiff clays tested under such high confining pressures.

The dependence of the material response on the axial strain rate is likely to indicate a significant influence of the loading frequency in stress-controlled fatigue tests. This would suggest that the cyclic behaviour of caprock materials should be studied experimentally using loading frequencies consistent with those expected in the field. However, hydrogen injection-production operations are characterised by very low frequencies, characteristic of the seasonality of renewable energy sources. Such frequencies are not compatible with feasible test times in the laboratory. Cyclic tests will therefore have to be performed at higher strain rates, but the results will necessarily have to be interpreted in the light of strain rate effects.

A potential approach to overcome the limitations associated with time constraints in fatigue life testing could be the explicit introduction of viscous effects in constitutive modelling. For this purpose, various approaches have already been shown to be effective in reproducing the experimentally observed response of geomaterials (e.g., [74,75]). These approaches should be coupled with modelling of the debonding mechanism to properly reproduce the observed fragile response of the caprock material (e.g., [76,77]). The constitutive parameters could then be calibrated against the results of tests conducted at different "affordable" strain rates, such as those presented in this research.

Another interesting emerging aspect is the observed variation of elastic wave velocities with progressive cyclic destructuration. As the material structure degrades, the P- and especially the S-wave velocities tend to decrease, dropping rapidly when cyclic failure occurs. At the same time, the failure of the specimen also induces a strong reduction in the maximum normalised cross correlation coefficient, which is probably related to the development of the shear band. It will be worthwhile in future research to evaluate whether monitoring the evolution of the elastic wave propagation characteristics can be a promising option for assessing in situ the progress of the destructuration process of the caprock formation in the vicinity of injection wells.

CRediT authorship contribution statement

Andrea Ciancimino: Conceptualization, Data curation, Investigation, Methodology, Visualization, Writing – original draft. **Renato Maria Cosentini:** Methodology, Writing – review & editing. **Sebastiano Foti:** Conceptualization, Funding acquisition, Project administration, Writing – review & editing. **Alessandro Messori:** Project administration, Writing – review & editing. **Hidayat Ullah:** Investigation, Writing – review & editing. **Giorgio Volonté :** Project administration, Writing – review & editing. **Guido Musso:** Conceptualization, Methodology, Supervision, Writing – original draft.

Declaration of Competing Interest

The authors declare that they have no known competing financial interests or personal relationships that could have appeared to influence the work reported in this paper.

Data Availability

Data will be made available on request.

Acknowledgments

Funding was provided by ENI SpA within the project “Hynergy”. The authors gratefully thank Eni SpA for the authorization to publish this work.

References

1. Engeland K, Borga M, Creutin J-D, François B, Ramos M-H, Vidal J-P. Space-time variability of climate variables and intermittent renewable electricity production – a review. *Renew Sustain Energy Rev*. 2017;79:600–617. https://doi.org/10.1016/j.rser.2017.05.046.
2. Heide D, von Bremen L, Greiner M, Hoffmann C, Speckmann M, Bofinger S. Seasonal optimal mix of wind and solar power in a future, highly renewable Europe. *Renew Energy*. 2010;35(11):2483–2489. https://doi.org/10.1016/j.renene.2010.03.012.
3. Heinemann N, Alcalde J, Miocic JM, et al. Enabling large-scale hydrogen storage in porous media - the scientific challenges. *Energy Environ Sci*. 2021;14(2):853–864. https://doi.org/10.1039/d0ee03536j.
4. Carr S, Premier GC, Guwy AJ, Dinsdale RM, Maddy J. Hydrogen storage and demand to increase wind power onto electricity distribution networks. *Int J Hydrog Energy*. 2014;39(19):10195–10207. https://doi.org/10.1016/j.ijhydene.2014.04.145.
5. Gahleitner G. Hydrogen from renewable electricity: An international review of power-to-gas pilot plants for stationary applications. *Int J Hydrog Energy*. 2013;38(5):2039–2061. https://doi.org/10.1016/j.ijhydene.2012.12.010.
6. Dincer, I. (2012). Green methods for hydrogen production. Paper presented at the International Journal of Hydrogen Energy.
7. Hosseini SE, Wahid MA. Hydrogen production from renewable and sustainable energy resources: promising green energy carrier for clean development. *Renew Sustain Energy Rev*. 2016;57:850–866. https://doi.org/10.1016/j.rser.2015.12.112.
8. Miller HA, Bouzek K, Hnat J, et al. Green hydrogen from anion exchange membrane water electrolysis: a review of recent developments in critical materials and operating conditions. *Sustain Energy Fuels*. 2020;4(5):2114–2133. https://doi.org/10.1039/c9se01240k.
9. Ali Khan MH, Daiyan R, Neal P, Haque N, MacGill I, Amal R. A framework for assessing economics of blue hydrogen production from steam methane reforming using carbon capture storage & utilisation. *Int J Hydrog Energy*. 2021;46(44):22685–22706. https://doi.org/10.1016/j.ijhydene.2021.04.104.
10. Howarth RW, Jacobson MZ. How green is blue hydrogen? *Energy Sci Eng*. 2021;9(10):1676–1687. https://doi.org/10.1002/ese3.956.
11. Muradov NZ, Veziroğlu TN. "Green" path from fossil-based to hydrogen economy: an overview of carbon-neutral technologies. *Int J Hydrog Energy*. 2008;33(23):6804–6839. https://doi.org/10.1016/j.ijhydene.2008.08.054.
12. Reiter G, Lindorfer J. Global warming potential of hydrogen and methane production from renewable electricity via power-to-gas technology. *Int J Life Cycle Assess*. 2015;20(4):477–489. https://doi.org/10.1007/s11367-015-0848-0.
13. Spataru C, Drummond P, Zafeiratou E, Barrett M. Long-term scenarios for reaching climate targets and energy security in UK. *Sustain Cities Soc*. 2015;17:95–109. https://doi.org/10.1016/j.scs.2015.03.010.
14. Reitenbach V, Ganzer L, Albrecht D, Hagemann B. Influence of added hydrogen on underground gas storage: a review of key issues. *Environ Earth Sci*. 2015;73(11):6927–6937. https://doi.org/10.1007/s12665-015-4176-2.
15. Tarkowski R. Underground hydrogen storage: characteristics and prospects. *Renew Sustain Energy Rev*. 2019;105:86–94. https://doi.org/10.1016/j.rser.2019.01.051.
16. Zivar D, Kumar S, Foroozesh J. Underground hydrogen storage: a comprehensive review. *Int J Hydrog Energy*. 2021;46(45):23436–23462. https://doi.org/10.1016/j.ijhydene.2020.08.138.
17. Stone, H.B.J., Veldhuis, I., Richardson, R.N. (2009). Underground hydrogen storage in the UK. In D. J. Evans & R. A. Chadwick (Eds.), Underground Gas Storage: Worldwide Experiences and Future Development in the Uk and Europe (Vol. 313, pp. 217–226).
18. Ozarslan A. Large-scale hydrogen energy storage in salt caverns. *Int J Hydrog Energy*. 2012;37(19):14265–14277. https://doi.org/10.1016/j.ijhydene.2012.07.111.
19. Heinemann N, Booth MG, Haszeldine RS, Wilkinson M, Scafidi J, Edlmann K. Hydrogen storage in porous geological formations - onshore play opportunities in the midland valley (Scotland, UK). *Int J Hydrog Energy*. 2018;43(45):20861–20874. https://doi.org/10.1016/j.ijhydene.2018.09.149.
20. Nordbotten JM, Celia MA, Bachu S, Dahle HK. Semianalytical solution for CO_2 leakage through an abandoned well. *Environ Sci Technol*. 2005;39(2):602–611.
21. Rutqvist J. The geomechanics of CO_2 storage in deep sedimentary formations. *Geotech Geol Eng*. 2012;30(3):525–551.
22. Capasso, G., Musso, G., & Mantica, S. (2008). Long-term stability study of open-hole completions in a producing hydrocarbon field. Paper ARMA 08–238, 42nd US Rock Mechanics Symposium and 2nd U.S.-Canada Rock Mechanics Symposium, San Francisco, June 29-July 2, 2008.
23. Martìn CM, Piqué TM, Pereira J-M, Manzanal DG. Performance of lightweight cement pastes under CO_2 storage conditions. *Proc 16th Greenh Gas Control Technol Conf (GHGT-16)*. 2022:23–24. Oct 2022.
24. Fjaer, E., Holt, R.M., Raaen, A.M., Risnes, R., Horsrud, P. (2008). Petroleum related rock mechanics. 2nd ed. Development in Petroleum Science, Vol. 53. Amsterdam, Holland.
25. Leung DYC, Caramanna G, Maroto-Valer MM. An overview of current status of carbon dioxide capture and storage technologies. *Renew Sustain Energy Rev*. 2014;39:426–443. https://doi.org/10.1016/j.rser.2014.07.093.
26. Berta M, Dethlefsen F, Ebert M, Schäfer D, Dahmke A. Geochemical effects of millimolar hydrogen concentrations in groundwater: an experimental study in the context of subsurface hydrogen storage. *Environ Sci Technol*. 2018;52(8):4937–4949. https://doi.org/10.1021/acs.est.7b05467.
27. Gregory SP, Barnett MJ, Field LP, Milodowski AE. Subsurface microbial hydrogen cycling: natural occurrence and implications for industry. art. no. 53 *Microorganisms*. 2019;7(2). https://doi.org/10.3390/microorganisms7020053.
28. Hettema MHH, Schutjens PMTM, Verboom BJM, Gussinklo HJ. Production-induced compaction of a sandstone reservoir: the strong influence of stress path. *SPE Reserv Eval Eng*. 2000;3(4):342–347. https://doi.org/10.2118/65410-PA.
29. Nagel NB. Compaction and subsidence issues within the petroleum industry: from Wilmington to Ekofisk and beyond. *Phys Chem Earth, Part A: Solid Earth Geod*. 2001;26(1-2):3–14. https://doi.org/10.1016/S1464-1895(01)00015-1.
30. Settari A, Walters DA. Advances in coupled geomechanical and reservoir modeling with applications to reservoir compaction. *SPE J*. 2001;6(3):334–342. https://doi.org/10.2118/74142-PA.
31. Musso G, Volonté G, Gemelli F, Corradi A, Nguyen SK, Lancellotta R, Brignoli M, Mantica S. Evaluating the subsidence above gas reservoirs with an elasto-viscoplastic constitutive law. Laboratory evidences and case histories. *Geomech Energy Environ*. 2021;28:2352–3808. https://doi.org/10.1016/j.gete.2021.100246, 100246, ISSN.
32. Lavrov, A. (2016). Dynamics of stresses and fractures in reservoir and cap rock under production and injection. Paper presented at the Energy Procedia.
33. Tenthorey E, Vidal-Gilbert S, Backé G, et al. Modelling the geomechanics of gas storage: a case study from the Iona gas field, Australia. *Int J Greenh Gas Control*. 2013;13:138–148. https://doi.org/10.1016/j.ijggc.2012.12.009.
34. Teatini P, Castelletto N, Ferronato M, et al. Geomechanical response to seasonal gas storage in depleted reservoirs: a case study in the Po River basin, Italy. *J Geophys Res: Earth Surf*. 2011;116(2):1–21. https://doi.org/10.1029/2010JF001793.
35. Yang S, Hu S, Qi Z, et al. Stability evaluation of fault in hydrocarbon reservoir-based underground gas storage: a case study of W gas storage. *Fuel*. 2024;357A. https://doi.org/10.1016/j.fuel.2023.129657.
36. Jeanne P, Zhang Y, Rutqvist J. Influence of hysteretic stress path behavior on seal integrity during gas storage operation in a depleted reservoir. *J Rock Mech Geotech Eng*. 2020;12(4):886–899. https://doi.org/10.1016/j.jrmge.2020.06.002.
37. Fan J, Liu W, Jiang D, Chen J, Tiedeu WN, Daemen JJK. Time interval effect in triaxial discontinuous cyclic compression tests and simulations for the residual stress in rock salt. *Rock Mech Rock Eng*. 2020;53(9):4061–4076. https://doi.org/10.1007/s00603-020-02150-y.
38. He M, Li N, Zhu C, Chen Y, Wu H. Experimental investigation and damage modeling of salt rock subjected to fatigue loading. *Int J Rock Mech Min Sci*. 2019;114:17–23. https://doi.org/10.1016/j.ijrmms.2018.12.015.
39. Rouabhi A, Hévin G, Soubeyran A, Labaune P, Louvet F. A multiphase multicomponent modeling approach of underground salt cavern storage. *Geomech Energy Environ*. 2017;12:21–35. https://doi.org/10.1016/j.gete.2017.08.002.
40. Song R, Yue-ming B, Jing-Peng Z, De-yi J, Chun-he Y. Experimental investigation of the fatigue properties of salt rock. *Int J Rock Mech Min Sci*. 2013;64:68–72.
41. Cafaro F, Cotecchia F. Structure degradation and changes in the mechanical behaviour of a stiff clay due to weathering. *Géotechnique*. 2001;51(5):441–453. https://doi.org/10.1680/geot.2001.51.5.441.
42. Cotecchia F, Cafaro F, Aresta B. Structure and mechanical response of sub-Apennine Blue Clays in relation to their geological and recent loading history. *Géotechnique*. 2007;57(2):167–180. https://doi.org/10.1680/geot.2007.57.2.167.
43. Amorosi A, Rampello S. An experimental investigation into the mechanical behaviour of a structured stiff clay. *Géotechnique*. 2007;57(2):153–166.
44. Burland J, Rampello S, Georgiannou V, Calabresi G. A laboratory study of the strength of four stiff clays. *Géotechnique*. 1996;46(3):491–514.
45. Benetatos C, Rocca V, Verga F, Adinolfi L, Marzano F. Deformation behavior of a regional shale formation from integrated laboratory and well data analysis: insights for underground fluid storage in northern Italy. *Geoenergy Sci Eng*. 2023;229,212109. https://doi.org/10.1016/j.geoen.2023.212109.
46. Eaton, B.A. (1975). The Equation for Geopressure Prediction from Well Logs. Society of Petroleum Engineers - Fall Meeting of the Society of Petroleum Engineers of AIME, FM 1975, doi:10.2523/5544-ms.
47. Eaton BA, Eaton TL. Fracture gradient prediction for the new generation. *World Oil*. 1997;218(10):93–100.
48. Scelsi G, De Bellis M, Pandolfi A, Musso G, Della Vecchia G. A step-by-step analytical procedure to estimate the in-situ stress state from borehole data. *J Pet Sci Eng*. 2019;176:994–1007.
49. Skempton A. The pore-pressure coefficients A and B. *Géotechnique*. 1954;4(4):143–147.
50. ASTM. *D5298-16 Standard Test Method for Measurement of Soil Potential (Suction) Using Filter Paper*. West Conshohocken, PA: ASTM International,; 2016.
51. Marinho FA, Oliveira OM. The filter paper method revisited. *Geotech Test J*. 2006;29(3):250–258.
52. ASTM. *D6836-16 Standard Test Methods for Determination of the Soil Water Characteristic curve for Desorption Using Hanging column, Pressure Extractor, Chilled Mirror, Hygrometer, or Centrifuge*. West Conshohocken, PA: ASTM International; 2016.

53. Doran IG, Sivakumar V, Graham J, Johnson A. Estimation of in situ stresses using anisotropic elasticity and suction measurements. *Géotechnique*. 2000;50(2): 189–196. https://doi.org/10.1680/geot.2000.50.2.189.
54. Lang A. Osmotic coefficients and water potentials of sodium chloride solutions from 0 to 40C. *Aust J Chem*. 1967;20(9):2017–2023.
55. Musso G, Cosentini RM, Foti S, Comina C, Capasso G. Assessment of the structural representativeness of sample data sets for the mechanical characterization of deep formations. *Geophysics*. 2015;80(5):D441–D457. https://doi.org/10.1190/geo2014-0351.1.
56. Barla G, Barla M, Debernardi D. New triaxial apparatus for rocks. *Rock Mech Rock Eng*. 2010;43(2):225–230. https://doi.org/10.1007/s00603-009-0076-7.
57. Lo Presti DCF, Pallara O, Cavallaro A, Jamiolkowski M. Influence of reconsolidation techniques and strain rate on the stiffness of undisturbed clays from triaxial tests. *Geotech Test J*. 1999;22(3):211–225. https://doi.org/10.1520/gtj11112j.
58. Barla M. Numerical simulation of the swelling behaviour around tunnels based on special triaxial tests. *Tunn Undergr Space Technol*. 2008;23(5):508–521. https://doi.org/10.1016/j.tust.2007.09.002.
59. Bonini M, Debernardi D, Barla M, Barla G. The mechanical behaviour of clay shales and implications on the design of tunnels. *Rock Mech Rock Eng*. 2009;42(2): 361–388. https://doi.org/10.1007/s00603-007-0147-6.
60. Wild KM, Barla M, Turinetti G, Amann F. A multi-stage triaxial testing procedure for low permeable geomaterials applied to Opalinus Clay. *J Rock Mech Geotech Eng*. 2017;9(3):519–530. https://doi.org/10.1016/j.jrmge.2017.04.003.
61. Bishop AW. The influence of system compressibility on the observed pore-pressure response to an undrained change in stress in saturated rock. *Géotechnique*. 1976;26 (2):371–375. https://doi.org/10.1680/geot.1976.26.2.371.
62. Wissa AE. Pore pressure measurement in saturated stiff soils. *J Soil Mech Found Div*. 1969;95(4):1063–1073.
63. Conte E, Troncone A. One-dimensional consolidation under general time-dependent loading. *Can Geotech J*. 2006;43(11):1107–1116. https://doi.org/10.1139/t06-064.
64. Head, K.H. (1998). Manual of soil laboratory testing (Vol. 3-Effective stress tests). West Sussex, UK: John Wiley and Sons, Inc.
65. ASTM. *D4767-11 Standard Test Method for Consolidated Undrained Triaxial Compression Test for Cohesive Soils*. West Conshohocken, PA: ASTM International,; 2020.
66. Augustesen A, Liingaard M, Lade PV. Evaluation of time-dependent behavior of soils. *Int J Geomech*. 2004;4(3):137–156.
67. Xiao J-Q, Ding D-X, Jiang F-L, Xu G. Fatigue damage variable and evolution of rock subjected to cyclic loading. *Int J Rock Mech Min Sci*. 2010;47(3):461–468.
68. Lefebvre G, LeBoeuf D. Rate effects and cyclic loading of sensitive clays. *J Geotech Eng*. 1987;113(5):476–489.
69. Sheahan TC, Ladd CC, Germaine JT. Rate-dependent undrained shear behavior of saturated clay. *J Geotech Eng*. 1996;122(2):99–108.
70. Vaid YP, Campanella RG. Time-dependent behavior of undisturbed clay. *J Geotech Eng Div*. 1977;103(7):693–709.
71. Guo Y, Yang C, Mao H. Mechanical properties of Jintan mine rock salt under complex stress paths. *Int J Rock Mech Min Sci*. 2012;56:54–61. https://doi.org/10.1016/j.ijrmms.2012.07.025.
72. Martin C, Chandler N. The progressive fracture of Lac du Bonnet granite. *Int J Rock Mech Min Sci Geomech Abstr*. 1994;31(6):643–659.
73. Xiao J-Q, Ding D-X, Xu G, Jiang F-L. Inverted S-shaped model for nonlinear fatigue damage of rock. *Int J Rock Mech Min Sci*. 2009;46(3):643–648.
74. Perzyna P. Fundamental Problems in Viscoplasticity. *Adv Appl Mech*. 1966;9(C): 243–377. https://doi.org/10.1016/S0065-2156(08)70009-7.
75. Vermeer, P., & Neher, H. (1999). A soft soil model that accounts for creep. Paper presented at the Beyond 2000 in computational geotechnics, Rotterdam.
76. Gens, A., & Nova, R. (1993). Conceptual bases for a constitutive model for bonded soils and weak rocks. Proceedings of geotechnical engineering of soft rocks-hard soils, A.A. Balkema, Rotterdam, Vol.1, 485–494.
77. Seidalinov G, Taiebat M. Bounding surface SANICLAY plasticity model for cyclic clay behavior. *Int J Numer Anal Methods Geomech*. 2014;38(7):702–724.